AGU100 ADVANCING EARTH AND SPACE SCIENCE

Paleoceanography and Paleoclimatology

RESEARCH ARTICLE
10.1002/2017PA003233

Last Millennium Meridional Shifts in Hydroclimate in the Central Tropical Pacific

Melinda C. Higley[1], Jessica L. Conroy[1,2], and Susan Schmitt[2]

[1]Department of Geology, University of Illinois Urbana-Champaign, Champaign, IL, USA, [2]Department of Plant Biology, University of Illinois Urbana-Champaign, Urbana, IL, USA

Key Points:
- A new lake sediment record from Kiritimati provides constraints on Intertropical Convergence Zone position during the last millennium
- Drier than modern conditions are inferred from 900 to 1200 CE, and a shift toward modern lake conditions begins at 1200 CE
- Shifts in the Intertropical Convergence Zone explain centennial variations in tropical hydroclimate for the central tropical Pacific

Supporting Information:
- Supporting Information S1
- Table S1
- Table S2
- Table S3
- Table S4
- Table S5
- Table S6
- Table S7

Correspondence to:
M. C. Higley,
mchigley@illinois.edu

Citation:
Higley, M. C., Conroy, J. L., & Schmitt, S. (2018). Last millennium meridional shifts in hydroclimate in the central tropical Pacific. *Paleoceanography and Paleoclimatology, 33*, 354–366. https://doi.org/10.1002/2017PA003233

Received 23 AUG 2017
Accepted 6 MAR 2018
Accepted article online 9 MAR 2018
Published online 6 APR 2018

Abstract Reconstructing past changes in the spatial structure of tropical Pacific hydroclimate requires archives of past moisture balance across spatial gradients of precipitation. To date, only one, 600-year, terrestrial record of hydroclimate is available for the central tropical Pacific (CTP) from Washington Lake, Washington Island, limiting the ability to test the hypotheses regarding the location of the CTP Intertropical Convergence Zone (ITCZ) in the last millennium. A new lake sediment record from Lake 30, Kiritimati, Republic of Kiribati, 3° south of Washington Island, provides additional constraints on past CTP ITCZ position. Lake 30 geochemical and sedimentological data indicate an episode of increased microbial mat development and gypsum precipitation from 900 to 1200 CE, coincident with the Medieval Climate Anomaly (MCA). We infer drier conditions during the MCA at Kiritimati as the Washington Lake proxy record indicates wetter conditions, suggesting that the CTP ITCZ was displaced northward during the MCA relative to its position today. At the transition between the MCA and the Little Ice Age (LIA), Lake 30 sediment becomes predominantly carbonate, suggesting a transition to wetter conditions and a southward shift of the ITCZ relative to its MCA position. However, a tropical Pacific synthesis of hydroclimate-sensitive proxy records does not point to a consistent spatial or temporal pattern of variability in the MCA and LIA, suggesting multiple influences on centennial-scale tropical Pacific hydroclimate during the last millennium.

1. Introduction

Tropical Pacific climate plays a critical role in shaping global climate variability (Trenberth, 2002). The most salient aspects of ocean-atmosphere circulation in this region, which alter large-scale rainfall patterns, include the seasonal, meridional movement of the Intertropical Convergence Zone (ITCZ), the Pacific Walker Circulation (PWC), and the interannual El Niño-Southern Oscillation (ENSO). Understanding the response of these systems to past changes in forcing, as well as their internal variability, is vital to inform the nature of future climate change in this region, which hosts a growing population vulnerable to limited water resources (Holding et al., 2016; United Nations, 2017). However, the location of the ITCZ, strength of the PWC, and ENSO variability during past periods with different background climate states remains uncertain.

There are varied hypotheses regarding drivers of centennial-scale hydroclimate variability in the tropical Pacific during the last millennium. A strengthened PWC has been suggested during the Medieval Climate Anomaly (MCA), from ~900 to 1300 CE (Graham et al., 2007). However, other records and syntheses purport the opposite (Yan, Sun, Oppo, et al., 2011). At the onset of the Little Ice Age (LIA; 1400 CE), a southward shift of the ITCZ is inferred from many hydroclimatic proxies across the tropics (Haug et al., 2001; Newton et al, 2006; Richey & Sachs, 2016; Sachs et al., 2009). In contrast, a contraction, rather than a southward shift, may have occurred in the western tropical Pacific at this time (Denniston et al., 2016; Konecky et al., 2013; Yan et al., 2015). Variability in the strength of the PWC may have also influenced tropical Pacific hydroclimate during the LIA. For example, western Pacific records indicate a wetter and fresher Indo-Pacific Warm Pool during the LIA, concomitant with some records from the eastern tropical Pacific suggesting relative dryness during the LIA—a spatial signature that is representative of the zonal PWC and is distinct from meridional ITCZ migration (Griffiths et al., 2016; Yan, Sun, Oppo, et al., 2011).

Disentangling the correct patterns and, subsequently, the mechanisms behind the last millennium hydroclimate variability in the tropical Pacific requires development of more paleoclimate records, especially in regions characterized by strong moisture gradients (e.g., Denniston et al., 2016). The Northern Line Islands in the central tropical Pacific (CTP), spanning 2° to 6°N, are an ideal location to develop such records, as the position of the ITCZ creates a sharp meridional rainfall gradient. Modern rainfall on Kiritimati (1.9°N,

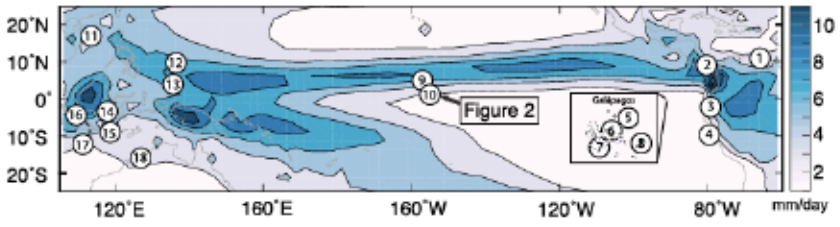

Figure 1. Mean annual precipitation (mm/day) across the tropical Pacific Ocean (1979–2010 CE; Adler et al., 2003). Circled numbers are referenced proxy locations. (1) %Ti, marine sediment, Cariaco Basin (Haug et al., 2001). Eastern Pacific: (2) Speleothem $\delta^{18}O$, Chilibrillo Cave (Lachniet, 2004); (3) red color intensity, lake sediment, Laguna Pallcacocha (Moy et al., 2002); (4) %lithic concentration, marine sediment, Peruvian shelf (Rein et al., 2004); (5) Ca-cps, scanning micro-XRF, Genovesa Crater Lake (Conroy et al., 2014); (6) PC1, scanning micro-XRF, Bainbridge Crater Lake (Thompson et al., 2017); (7) δD_{water} reconstruction from δD_{C24OL} and diatom assemblages, lake sediment, Poza de las Diablas, Galápagos (Nelson & Sachs, 2016). From El Junco, Galápagos, lake sediment: (8a) %sand (Conroy et al., 2008); (8b) ratio of tychoplanktonic to epiphytic diatoms (*T/E*; Conroy et al., 2009); (8c) $\delta D_{botryococcene}$ (Sachs et al., 2009); (8d) $\delta D_{dinosterol}$. (Atwood & Sachs, 2014). Central Pacific: (9) δD total lipid extracts, lake sediment, Washington Island (Sachs et al., 2009); (10) Lake 30, this study. Western Pacific: (11) Mean grain size, Cattle Pond, Dongdao Island (Yan, Sun, Oppo, et al., 2011); (12) $\delta D_{dinosterol}$, Spooky Lake, Palau (Sachs et al., 2009); (13) $\delta D_{dinosterol}$, Clear Lake, Palau (Richey & Sachs, 2016); (14) $\delta D_{leaf\ wax}$, marine sediment, Makassar Strait (Tierney et al., 2010); (15) $\delta^{18}O$ speleothem, Liang Luar Cave, Flores Island (Griffiths et al., 2016). From East Java, Indonesia: (16) $\delta D_{leaf\ wax}$, Lake Lading (Konecky et al., 2013); (17) %TIC from Lake Logung (Rodysill et al., 2012); (18) speleothem $\delta^{18}O$, KNI-51, northwest Australia (Denniston et al., 2016).

157.4°W) averages 2 mm/day, as the island is south of the ITCZ (Figure 1). Further north, precipitation rapidly increases to >6 mm/day at Washington Island (4.7°N, 160.4°W), which lies underneath the ITCZ.

In the semiarid conditions at Kiritimati, precipitation minus evaporation ($P - E$) influences the water and sediment chemistry of the numerous lakes found across on the island, which range from brackish to hypersaline (Saenger et al., 2006). Sediment records from closed basin, saline lakes can archive variability in hydroclimate through changes in mineralogy and sediment geochemistry (e.g., Dix et al, 1999). Minerals precipitated in saline lakes reflect the ionic composition of the lake water, making saline lakes sensitive recorders of environmental conditions (Eugster & Hardie, 1978). In fact, such "chemical" sediments have been considered one of the most sensitive proxies for climate (Schnurrenberger et al, 2003). According to the brine evolution pathways of Eugster and Hardie (1978), as a brine becomes enriched due to loss of water, typical authigenic precipitates initially include low-magnesium calcite, high-magnesium calcite, and aragonite, followed by other minerals such as gypsum and halite, dictated by lake water ionic composition and concentration. Thus, mineral precipitates preserved in lake sediments reflect the evolution of the saline lake water chemistry, which is frequently driven by water balance and $P - E$ in closed basin lakes.

This study presents the first well-dated lake sediment record from Kiritimati. We use this record of past changes in sediment mineralogy and geochemistry to assess island hydroclimate variability over the last millennium. To substantiate that the sediment record reflects the hydroclimate, we model evaporation-influenced mineralogy trends and compare sediment mineralogy and geochemistry with surface sediments and lake waters in modern Kiritimati lakes. We then compare our new record with the record from Washington Island, along with other hydroclimate proxy records from across the tropical Pacific, to describe the observed pattern of change in the tropical Pacific hydroclimate over the last millennium.

2. Materials and Methods

2.1. Surface Water Chemistry

In July 2014 we collected surface water and surface sediment samples from 26 lakes, 1 spring, the main lagoon, and the seawater from the northwestern shore of Kiritimati to measure the properties of water and sediment end members around the island. Water samples for cation analysis were filtered in the field with 0.22-μm filters and stored refrigerated in the dark in pre-acidified amber plastic bottles, unopened, until analysis. Water samples from Lake 30, the ocean, and lagoon were also analyzed for anions. The concentration of major cations was measured using inductively coupled plasma optical emission spectrometer (Perkin-Elmer, Optima 5300 DV; ±3%) at the University of Arizona. The concentration of major anions was measured with Dionex ICS 3000 gas chromatograph (±4% for Cl^-, SO_4^{2-}; ±2% for Br^-; ±2% F^-). A YSI Professional Plus multiparameter datasonde was used to collect temperature (±0.2 °C), conductivity (±0.5% of measurement in μS/cm), pH (0.01 units), and dissolved oxygen (± 2%). Salinity in parts per thousand was calculated from these data using the Gibbs Sea Water Oceanographic Toolbox (McDougall & Barker, 2011). Alkalinity was measured

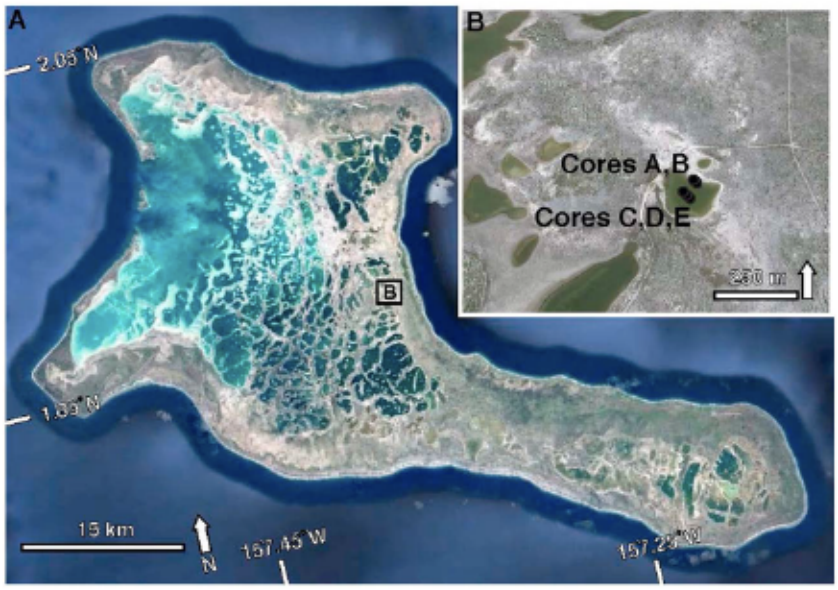

Figure 2. Location of Kiritimati Island and Lake 30 (B). (A) Aerial photograph of Kiritimati Island (Google Earth, 2017). (B) Lake 30 (1.873°N, 157.355°W) and surrounding landscape (Google Earth, 2017) with core sites (black dots).

onsite using a Hach Company alkalinity test kit. All chemistry data can be found in the supporting information, Table S1.

2.2. Sediment Cores

In July 2014 we collected five cores from Lake 30 (1.873°N, 157.355°W), which is approximately 5,800 m^2, sits ~3.0 m asl, and is 1.2 km from the eastern shoreline of Kiritimati (Figure 2). The area surrounding the lake is a flat, hardpan surface. A modified Livingstone piston corer was used to collect three overlapping cores, within a 2-m distance, in the center of the lake (cores C, D, and E, Figure 2). Duplicate intact sediment-water interface cores were collected using push cores 40 m from the Livingstone coring location (cores A and B, Figure 2). Due to the unconsolidated nature of the uppermost sediment, the upper 0.5 cm of each surface-water interface core was extruded into Whirl-Pak bags in the field. Livingstone cores were extruded in the field, and a Bolivia modification was used on four drives (Wright, 1967). These cores remained in polycarbonate tubing. The deepest drive does not include the end of the sediment package, which was not collected and is beyond the scope of the current investigation. Cores were transported to LacCore, the National Lacustrine Core Facility at the University of Minnesota, where they were split, described, digitally photographed, and scanned with a Geotek multisensor core logger for the whole core loop sensor and split core point sensor magnetic susceptibility, gamma density, electrical resistivity, and color spectrophotometry.

2.3. Chronology

The chronology for Lake 30 was constructed for the upper 120 cm of the composite core with seven radiocarbon dates (Table 1). An age model was created using Bacon 2.2 (Figure 3 and supporting information, Table S7; Blaauw & Christen, 2011). Samples were pretreated with standard HCl-NaOH-HCl for organic samples and 50% NaClO for the carbonate mud sample, combusted, and graphitized at the Illinois State Geological Survey, and ^{14}C measurements were conducted at the Keck-CCAMS, University of California. The modern (core top) date was calibrated using the CALIBomb program using the IntCal13 prebomb calibration curve (Reimer et al., 2013) and the NHZ3 postbomb calibration data set, which spatially overlaps our study area (Hua et al., 2013). A reservoir effect of 58 years was determined with the age of core top organic matter (Table 1). The reservoir effect was applied to the ages of four desiccated cyanobacterial mats, along with an uncertainty of ±50 years. The carbonate mud sample at the bottom of the studied core interval (121 cm) is lagoonal, rather than lacustrine, and was thus calibrated using the Marine13 calibration curve and a Delta *R* of 10 ± 15 (Zaunbrecher et al., 2010). The remaining ages were calibrated with the IntCal13 curve, and the age-depth relationships were modeled with the Bayesian model Bacon 2.2 (Blaauw &

Table 1
Radiocarbon Dates for Lake 30 Cores

Lab no.	Section depth (cm)	Composite depth (cm)	Core name	Material dated	$\delta^{13}C$	Fraction Modern Carbon	^{14}C year BP	^{14}C error	Calibration curve	Selected 2σ age range (cal year CE)	Rel. area under prob. distribution	Median prob. (cal year CE)	With res. effect (cal year CE)
ISGSA3470	0.0–0.5	0.0–0.5	K614-1A-1P	Organics (core top)	−18.7	0.9972 ± 0.0014	20	±15	IntCal13 prebomb	1955–1956	1.00	N.A.	−64
ISGSA3591	27.5	14	K614-1B-1P	Microbial mat	−15.2	0.9208 ± 0.0016	660	±15	IntCal13	1360–1386	0.50	1352	1410
ISGSA3432	45.5	35	K614-1A-1P	Seed	−25	0.9012 ± 0.0015	835	±15	IntCal13	1169–1250	1.00	1210	1268
ISGSA3590	16	49	K614-2C-1 L	Microbial mat	−16.1	0.8998 ± 0.0016	850	±15	IntCal13	1162–1221	1.00	1194	1252
ISGSA3506	23	73	K614-2D-1B	Microbial mat	−25.3	0.8601 ± 0.0015	1210	±15	IntCal13	769–882	1.00	821	879
ISGSA3430	4	111	K614-2C-3 L	Microbial mat	−12.3	0.8263 ± 0.0013	1530	±15	IntCal13	531–585	0.67	543	601
ISGSA3461	14	121	K614-2C-3 L	Carbonate mud	1.7	0.7375 ± 0.0011	2445	±15	Marine13	196–40 BCE	1.00	−125	N.A.

Note. Core names correspond to cores pictured in the supporting information, Figure S2. N.A. = not applicable.

Christen, 2011; Reimer et al., 2013). Based on our age model, the sedimentation rate from 0 to 14 cm is 0.02 cm/year, 14 to 111 cm is 0.12 cm/year, and abruptly changes to 0.01 cm/year at the transition from the laminated sediment to white authigenic carbonate mud.

2.4. X-Ray Fluorescence and Bulk Powder X-Ray Diffraction

Sediment elemental abundances were measured with an X-ray fluorescence (XRF) Itrax Corescanner (University of Minnesota-Duluth) with a molybdenum tube and 60 s dwell time. XRF data resolution is 1 cm for massive, nonlaminated sections and 1 mm to 500 μm for laminated sections. The XRF data are reported in counts per second and are normalized to coherent scatter. X-ray diffraction (XRD) on representative samples from the Lake 30 cores and surface sediment collected from other lakes provides mineralogical context for interpretation of the XRF elemental data. Wet samples of sediment were gently crushed with an agate mortar and pestle to break up aggregates and separate microbial material from mineral material. Gentle crushing, decanting, and centrifuging separated most of the organic microbial gels from the mineral component of the sample. Samples were sieved through 2 mm sieve to separate out biogenic carbonates, but mineral aggregates larger than 2 mm were crushed and returned to sample. The <2 mm mixture was centrifuged in deionized water for 10 min at 2,800 rpm, three times, to remove soluble salts (Cook et al., 1975; Last & Smol, 2001). Dry samples were ground into a powder with an agate mortar and pestle (Cook et al., 1975) and sieved through the 125-μm (#120) sieve size. The samples were run on a Siemens-Bruker D5000 at the Frederick Seitz Materials Research Laboratory at the University of Illinois with the following settings: incident angle of 5° to 90°, increment of 0.02, and scan speed of 1°min^{-1}. Results were analyzed in the Jade XRD software (supporting information, Figure S3).

2.5. Loss on Ignition

Loss on ignition was performed on the sediment cores as well as on surface samples from regional lakes to obtain the relative abundance of organic matter, carbonate, and the residual (Dean, 1974; Last & Smol, 2001). Approximately 0.5-cm^3 sediment samples were collected at 1-cm resolution. All wet samples were rinsed multiple times with deionized water to remove glutaraldehyde (used to fix surface sediment) and pore water containing sulfates, which can confound estimates of organic matter and carbonate. Sediment was dried at 120 °C overnight. After desiccation, dry sediment was transferred to clean dry crucibles and weighed. Samples were burned at 550 °C for 2 hr in a muffle furnace to remove organic content. Lids were placed on the crucibles beforehand to prevent flying ash. The crucibles were transferred to a desiccator until cool enough to weigh accurately. Samples were then burned at 1050 °C for 4 hr to remove carbonate. They were left in the furnace for a few hours to cool before being transferred to the desiccator for complete cooling. Percent organic content, carbonate, and the residual were calculated based on the mass of the combusted material relative to the original, dry mass. See supporting information for equations used to calculate loss on ignition.

2.6. Microbial Mat Frequency

Buried microbial mats occur throughout the top 120 cm of the sediment record. We visually identified 12 cohesive, finely laminated microbial mats in the sediment record and established the depth and age of each one. Mats were identified as sections of submillimeter dark and colorful laminations, high organic content, and a wavy contact with the sediment above and below. We only counted mats that were continuous across the width of the core with a defined structure and a clear top and bottom. Reported depth indicates the center of the mats. The mean age and 2σ error for the microbial mats was established in Bacon 2.2 (Blaauw & Christen, 2011) with the function Bacon.hist (depth).

2.7. Evaporation Model

Reaction path models were computed to demonstrate the saturation status of minerals in the Lake 30 water over the course of simulated evaporation, as we hypothesize that periods of lower $P - E$ drove gypsum precipitation in Lake 30. We performed the simulations using The Geochemist's Workbench® version 11.0 (Bethke & Yeakel, 2016a, 2016b) with 2014 field data (this study) and August 2002 data (Arp et al., 2012) for Lake 30. To compare system end members, we

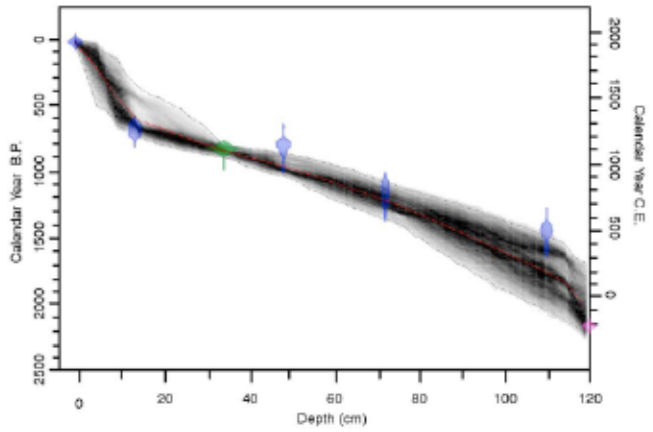

Figure 3. Age model for Lake 30. The age model is based on seven ^{14}C ages measured on aquatic material (organics and microbial mats, in blue) and carbonate mud (pink) with reservoir correction, and a terrestrial macrofossil (seed, green). The shaded gray areas indicate more likely calendar ages, gray stippled lines show 95% confidence intervals, and red curve shows the weighted mean age for each depth.

also modeled ocean water, a hypersaline lake (Lake 22 from Arp et al., 2012), and groundwater from a village well (Arp et al., 2012). The output of the model, the saturation index (SI) where positive values indicate supersaturation and negative values indicate undersaturation, are used to interpret the authigenic mineral precipitates observed in Lake 30 core sediments. For model details, settings, and input data, see the supporting information.

3. Results

Modern Kiritimati surface waters range from brackish to hypersaline (Table S1). The surface sediment of brackish lakes, such as Lake 30, is predominantly calcite ($CaCO_3$), aragonite, and high-Mg calcite, whereas the surface sediments of hypersaline lakes contain these minerals as well as gypsum ($CaSO_4{\cdot}H_2O$; supporting information, Figure S3) and cohesive, laminated, microbial mats. The core sediments from Lake 30 were divided into eight primary units based on sediment lithology (Figure 4 and see supporting information Figure S1). Unit I (0–7 cm) consists of brown, green, and pink thin-bedded micritic calcite mud with frequent carbonate sand grains. The topmost (0.5 cm) sediment of Lake 30 was a brown/green calcite mud with a density similar to the lake water. Unit II (7–31 cm) is represented by pink and light brown very thin bedded carbonate sand in a matrix of micritic carbonate mud, including fragmented brown laminated cyanobacterial mats at 13 and 21 cm (~0.5–2 cm thick). Pink laminated micritic calcite mud with frequent carbonate sand grains comprises Unit III (31–41 cm), with laminated cyanobacterial mats occurring at 32 and 38 cm (~0.5–2 cm thick). Unit IV (41–70 cm) consists of white and light brown laminated to very thin-bedded gypsum sand with calcite and aragonite mud, with laminated brown and green cyanobacterial mats occurring at 50, 53, 58, and 67 cm (~0.5–2 cm thick). Unit V (70–109 cm) contains pink, red, and green laminated micritic aragonite mud, with brown, light brown, and green laminated cyanobacterial mats at 77, 84, 100, and 104 cm (~0.5–2 cm thick). Unit VI (109–120 cm) contains light brown, thin-bedded carbonate sand in a matrix of carbonate mud. At 120 cm there is a sharp transition to white massive carbonate mud with gastropod and bivalve shells and fragments, which defines Unit VII (120–140 cm). Based on our age model, this transition occurs around 200 CE. Given the possible presence of a hiatus of uncertain duration at this transition zone and our focus on the last millennium, we only interpret the sediment record above this boundary. A gradual transition occurs between Unit VII and Unit VIII (140–400 cm), white massive carbonate mud.

Mineralogical differences between the carbonate mud and evaporite sand/mat unit are apparent in XRF S/Ca data (Figure 5). S/Ca values are continuously low from 200 to 890 CE, elevated from 890 to 1020, 1030 to 1060, and 1060 to 1200 CE, and low from 1200 to 1600 CE. S/Ca increases from 1850 CE to present but never approaches 890–1200 CE values. Where values of S/Ca are highest, we find gypsum crystals co-occurring with carbonate crystals in smear slides, gypsum sand in sediment samples, and gypsum in XRD. Gypsum is not detected at intervals above or below 900–1200 CE, where S/Ca is relatively low. The LOI % residual closely tracks S/Ca data (Figures 5 and 6), suggesting it also reflects gypsum abundance. Sr/Ca peaks occur in the sediment record corresponding to white laminations within or adjacent to microbial mats. Significant Sr/Ca peaks occur most frequently from 900 to 1230 CE corresponding to white laminations in the core sediment (Figure 6) and aragonite in smear slides (Figure 4), with the last peaks occurring near 1400 CE (Figure 5). The peaks in Sr/Ca represent an increase in aragonite relative to calcite due to the enhanced ability of Sr^{2+} to substitute for Ca^{2+} in aragonite (Kinsman & Holland, 1969). Cohesive laminated microbial mats first appear at ~400 CE and occur most frequently in Unit IV at multidecadal intervals until from ~650 to ~1200 CE with the last mat occurring at 1490 ± 190 CE (Figure 5, supporting information, Table S3). Taken together, these results show large changes in sediment characteristics over the last millennium, especially from 900 to 1200 CE, when the sediment is defined by microbial mats and coarser, gypsum-rich sediment. The combined S/Ca, Sr/Ca, and buried mat data indicate a transition period from 1200 to 1400 CE, at which time the sediment takes on characteristics that continue to the present-day. The sedimentation rate is faster from 900 to 1200 CE, with growing

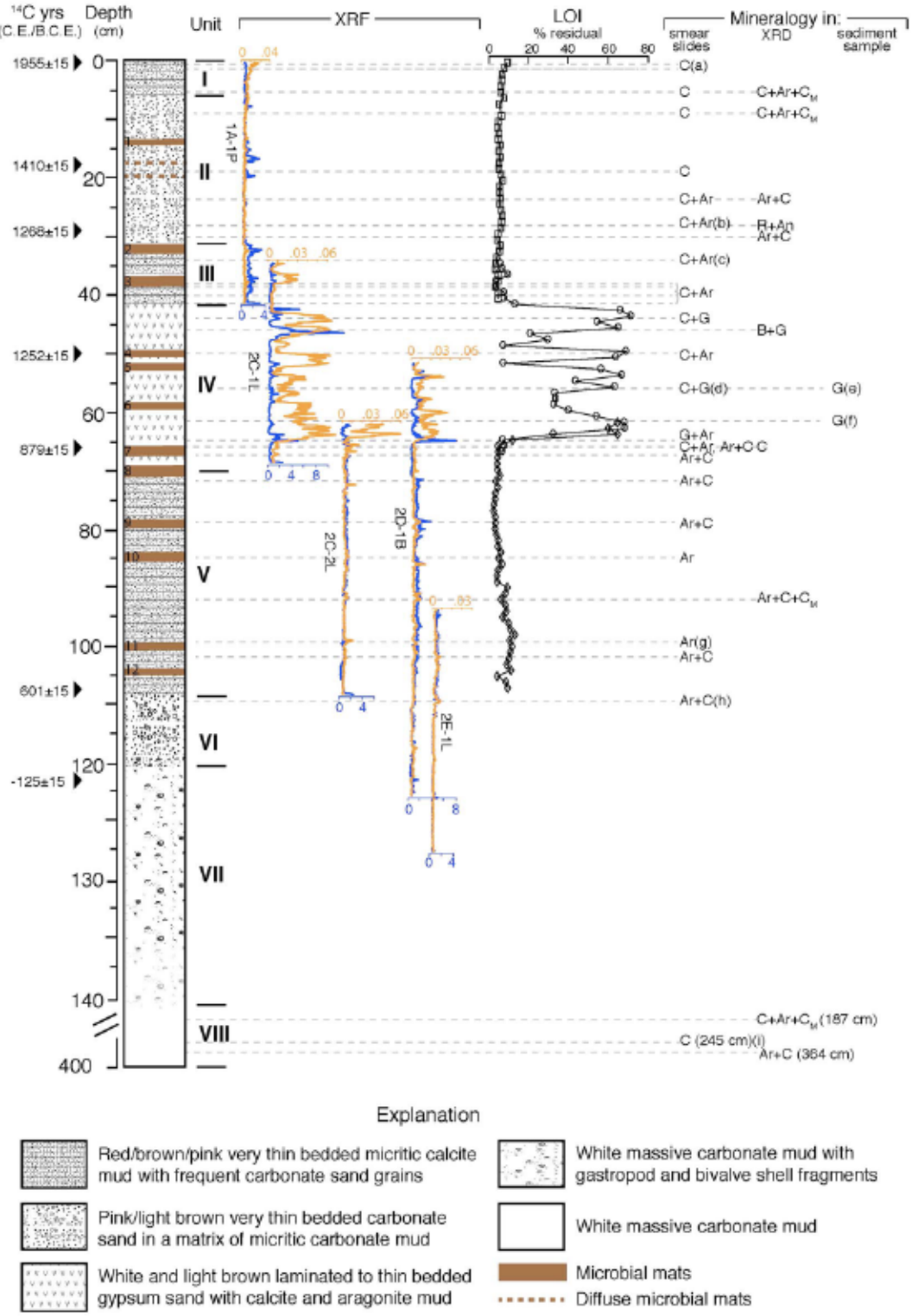

Figure 4. Lake 30 composite core lithology, X-ray fluorescence (XRF), loss on ignition (LOI), and mineralogical data. Triangles indicate calibrated radiocarbon ages. XRF data for S/Ca (orange) and Sr/Ca (blue) are shown for cores 1A-1P, 2C-1L, 2C-2L, 2D-1B, 2E-1L, from left to right. LOI data for three cores are indicated with squares, 1A-1P; circles, 2C-1L; and diamonds, 2C-2L. Mineralogy of core material is shown with smear slides observations, X-ray diffraction analysis, and sediment samples; dashed lines indicate depth of sample in the composite core. Ar = aragonite, An = ankerite, B = brushite, C = calcite, G = gypsum. C_M = Mg-calcite, R = rhodochrosite. Small case letters correspond to pictures in supporting information, Figure S1. Numbers next to microbial mats correspond to Table S3 in the supporting information. XRF and LOI data in this figure can be found in the supporting information.

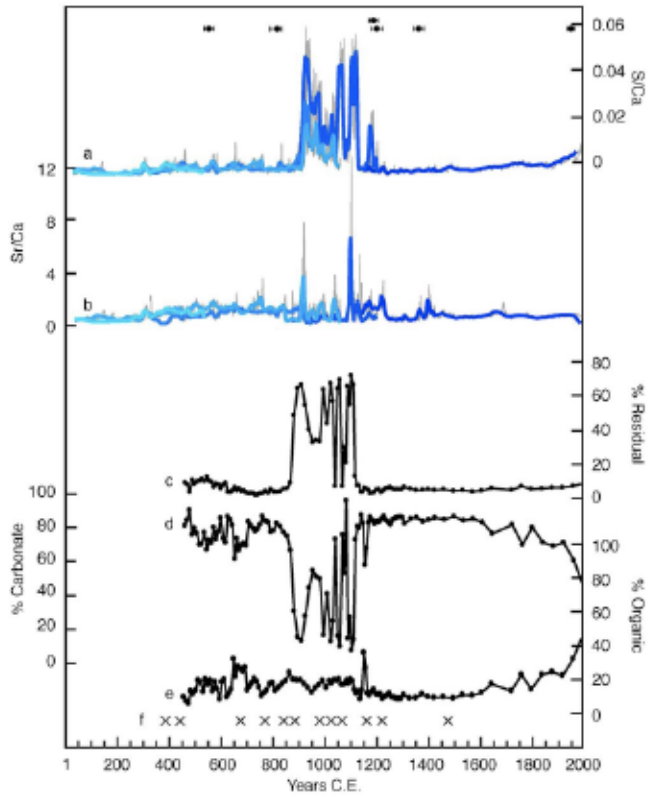

Figure 5. Kiritimati Lake 30 sediment record. (a) S/Ca, (b) Sr/Ca. Different shades of blue represent overlapping cores with 10-point running average, from darkest to lightest cores are 1A-1P, 2C-1L, 2D-1B, 2C-2L, and 1E-1L; raw data in gray. Percentage loss on ignition: (c) residual, (d) carbonate, (e) organic. (f) Ages of microbial mats. Location of ^{14}C ages $\pm 1\sigma$ plotted at top. The data used to construct this figure can be found in the supporting information, Tables S3, S5, and S6.

microbial mats and coarser particle size taking up more "space" in comparison to the period from 1200 CE to present, when the Lake 30 sediment record consists of fine-grained carbonate, with reduced pore space and fewer or absent microbial mats (Figure 3). In particular, the microbial mats are thick and hydroscopic and lack compressibility, compared to the fine carbonate sediment section of the core.

In our mineralogy modeling exercises, the output of the evaporation model is the SI, where positive values indicate supersaturation and negative values indicate undersaturation. In Lake 30, calcite and aragonite have SI values >0 and approach SI = 0 as water is removed. In contrast, the gypsum SI is lower under initial conditions but increases toward SI = 1 with increasing evaporation. This follows the model of Eugster and Hardie (1978) for evaporation of lake brines, which results in authigenic precipitates including low-magnesium calcite, high-magnesium calcite, and aragonite, followed by other minerals, such as gypsum and halite, dictated by lake water ionic composition and concentrations. Ocean water behaves similarly to Lake 30 water under simulated evaporation. In contrast, for the village well, evaporation has little effect on the saturation indices, until the last few steps, where gypsum approaches 1 after 90% water removal. All data, metadata, and simulations developed in this study are located either in the main text or as supporting information.

4. Discussion

4.1. Environmental Information in Lake 30 Sediment Variability

As we only detect microbial mats and gypsum in modern hypersaline lakes, the presence of microbial mats, gypsum, and increased aragonite relative to calcite from 900 to 1200 CE indicates more saline conditions in Lake 30, relative to modern. Today, brackish Lake 30 is an outcropping of groundwater defined by a freshwater lens overlying seawater (Arp et al., 2012). Periods of reduced ($P - E$) should manifest as increasingly saline groundwater, as the thickness of the freshwater lens decreases (Falkland & Woodroffe, 1997). Thus, we infer that this period, which falls within the MCA, was more arid on Kiritimati. It is unlikely the MCA was a period of increased lake salinity due to sea level rise, as estimates of sea level from fossil corals across Kiritimati reveal no significant sea level change for the last 5,000 years (Woodroffe et al., 2012). Lake 30 is also isolated from lakes connected to the lagoon. Sediment from lakes in contact with the lagoon (i.e., with a greater contribution from seawater) often contain more white carbonate precipitate (Saenger et al., 2006). We would expect higher sea level and surface seawater intrusion to be reflected as fine white sediment rather than increased gypsum and microbial

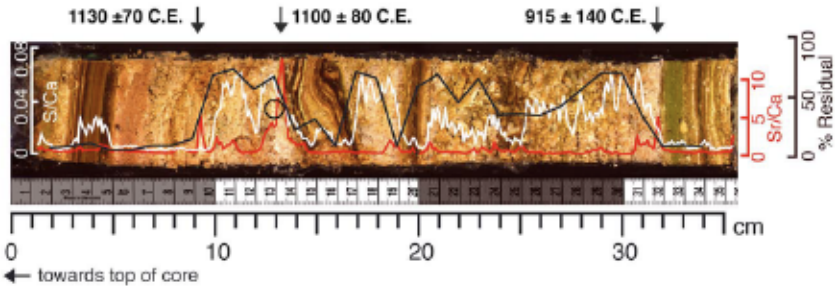

Figure 6. Image of core section K2014-K614-2C-1L with X-ray fluorescence and loss on ignition data superimposed to match the time series data with a visual of the core material (S/Ca, white; Sr/Ca, red; %residual, black). Black circle indicates depth of gypsum detected in X-ray diffraction. Arrows indicate dates interpolated from age model, corresponding to Sr/Ca peaks.

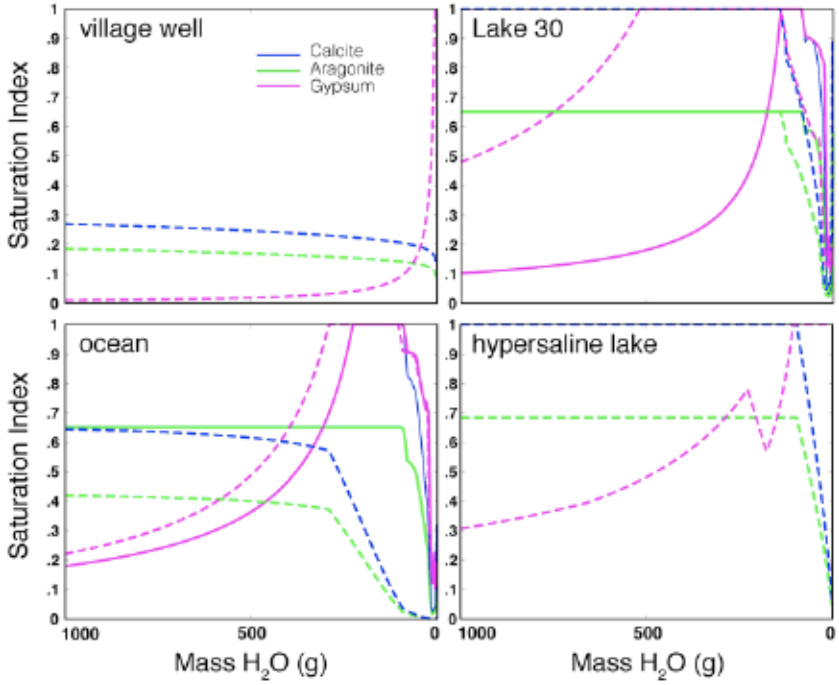

Figure 7. The Geochemist's Workbench® evaporation models based on the chemistry of ground water from a well, brackish Lake 30, the ocean, and hypersaline lake. Solid lines are data from this study, and dashed lines are data from 2002 (Arp et al., 2012). For the well and hypersaline lake, data are only from 2002. Mineral saturation status is indicated by the saturation index, where positive values indicate supersaturation and negative values indicate undersaturation.

mats. Comparing the results for 2014 Lake 30 water chemistry versus 2002, a drier period (supporting information, Figure S4), the gypsum SI ≈ 1 after only 48% water removal, versus 90% in 2014 (Figure 7). Therefore, not only is evaporation a viable path to precipitate gypsum in Lake 30 but precipitation of gypsum is enhanced with more saline initial water chemistry after a period of lower rainfall (supporting information, Table S4).

4.2. Testing the Hypothesis of CTP ITCZ Migration

The inferred centennial periods of fresher and more saline lake water during the last 2,000 years from Lake 30 improve constraints on the past position of the ITCZ in the CTP. In order to test the hypothesis that the ITCZ migrated during the last millennium, we compare the only two sediment records available for the CTP, from Lake 30 and Washington Lake, Washington Island. Located north of Kiritimati, Washington Island currently sits under the ITCZ. As a result, today Washington Lake is a freshwater lake surrounded by heavy vegetation, and organic-rich gyttja sediment accumulates at the lake bottom (Saenger et al., 2006). The 9-m sediment record from Washington Lake consists of modern organic gyttja overlying red microbial mats, ending with white carbonate mud that extends to bedrock. Hypersalinity during the majority of the last millennium is inferred from the presence of the salt-tolerant microbial communities, and hydrogen isotope ratios from this same unit indicate drier conditions from 1420 to 1640 CE (Sachs et al., 2009). This period of higher inferred salinity and aridity is thought to reflect a migration of the ITCZ south of the site during the LIA.

The period of higher inferred aridity on Kiritimati from 900 to 1200 CE, followed by a transition period between 1200 and 1400 CE back to more humid conditions, suggests that the ITCZ must have been positioned further from Kiritimati during the MCA. Combined with the Washington Lake record, it is likely the ITCZ was in a more northerly position than today (Figure 8). Our inability to find material to date during the LIA period precludes our interpretation of this period. The gradual shift between 1200 and 1400 CE to sediments similar to modern in Lake 30 suggests a southward shift of the ITCZ near the beginning of the LIA, relative to its more northerly position during the MCA; however, at centennial scales, from 1200 CE to present, Lake 30 does not display major sedimentological regime changes. Notably, there is no organic gyttja in the 2,000-year-long Lake 30 sediment record, similar to the sediment accumulating today on Washington

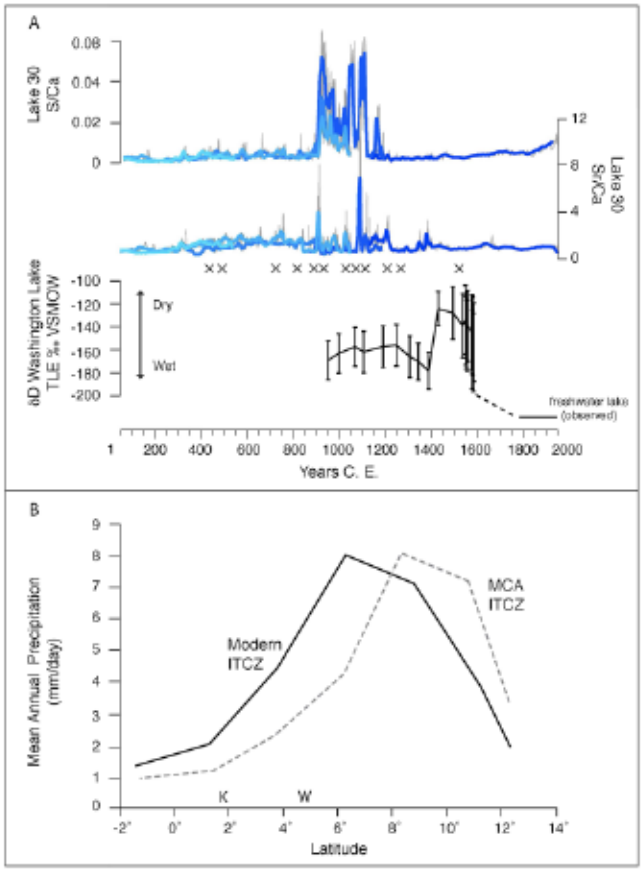

Figure 8. (a) Comparison of central tropical Pacific lake records. S/Ca and Sr/Ca from Lake 30 overlapping cores (blue lines) and δD from Washington Lake (black line; Sachs et al., 2009). (a) Schematic of mean annual modern (1979–2016 CE) precipitation (mm/day) averaged from 160°W to 150°W (solid line, Adler et al., 2003). Dashed line indicates the proposed northward shift of Intertropical Convergence Zone (ITCZ) during the Medieval Climate Anomaly (MCA). K = Kiritimati Island, TLE = total lipid extracts, W = Washington Island, VSMOW = Vienna Standard Mean Ocean Water.

Island; therefore, it is unlikely that the ITCZ sat directly over Kiritimati for a prolonged period of time during the last 2,000 years. Neither the dry period marked at 1420 CE or the current wet period on Washington Island (1800 CE to present) seem to be reflected as coeval centennial hydroclimate anomalies at Kiritimati (Figure 8). We note that seasonal variations in the ITCZ (Dima & Wallace, 2003) could play a role in determining more nuanced interpretations of the past location of the ITCZ in the CTP, but given the lack of knowledge about specific seasonal biases in most time-averaged sediment records, including our own, here we focus on the mean annual position. In sum, despite the lack of clear evidence for the mean location of the CTP-ITCZ during the LIA, the inferred wet/dry transition at Washington Island and dry/wet transition at Kiritimati from 1200 to 1400 CE still attests to a hydroclimate shift between the MCA and the transition into the LIA in the CTP. In the following sections, we examine the current catalogue of tropical Pacific hydroclimate records spanning the past two millennia to test if the observed CTP spatiotemporal hydroclimate patterns are consistent across the tropical Pacific.

4.3. Centennial Variations in Tropical Precipitation in the Last Millennium

Although the migration of the ITCZ can explain the MCA and MCA to LIA transition in the CTP, it may not be sufficient to explain hydroclimatic patterns across the tropical Pacific. To assess larger, pan-tropical Pacific spatial patterns of hydroclimate change, we plot the Z scores of 21 hydroclimate-sensitive proxy records, averaged into century-long intervals (Figure 9). In the case of papers or records where multiple proxies were measured, we select a variable that supports the original author's interpretations (Table S8). Z scores were calculated with the 1–2000 CE long-term mean and standard deviation, or the long-term mean and standard deviation of the record, if shorter. Taking all the tropical Pacific hydroclimate records at centennial-scale resolution as plotted in Figure 9, no consistent pattern of hydroclimatic change emerges during the 400-year averaged MCA and LIA periods (Figure 10). To further test the main hypotheses proposed for tropical Pacific hydroclimate change during the MCA and LIA, we also compare observed wet and dry anomalies from Figure 9 for the MCA and LIA versus expected wet and dry anomalies if the ITCZ had migrated, expanded/contracted, or if PWC strengthened/weakened during these two periods (supporting information, Tables S8 and S9). These results are summarized in Table 2, where we show percent agreement as well as the categorical agreement index, Cohen's κ, which, unlike the simpler percent agreement, also accounts for agreement due to chance (Cohen, 1960). Percent agreement ranges from 35% to 65%, and when also accounting for agreement due to chance, agreement is more limited, with low κ values overall (perfect agreement is represented by a value of $\kappa = 1$). This may be partly due to oftentimes large differences in the timing of wet and dry anomalies, which rarely adhere to the typical time spans allocated to the MCA and LIA. This ultimately produces small average Z scores when a period has both a wet and dry anomaly. Thus, we also calculated agreement indices using only MCA and LIA averages for those records where average MCA and LIA Z scores were $>|0.2|$. Yet we still find weak support for all the proposed hypotheses, in both percent agreement (38–64%) and Cohen's κ, although we note that the highest agreement is for an LIA ITCZ shift. However, overall, the relatively low values for all hypotheses lead us to conclude that we are not able to attribute tropical Pacific hydroclimatic variability over the last millennium to one mechanism.

The proposed forcing factors behind the changes in the last millennium tropical Pacific hydroclimate include hemispheric temperature gradients, solar variability, and volcanic forcing. Interhemispheric energy imbalance is thought to play a role in ITCZ shifts (Schneider et al., 2014). Such ITCZ movements of the last millennium may be externally forced, via the influence of volcanic aerosol or solar forcing amplifying internal

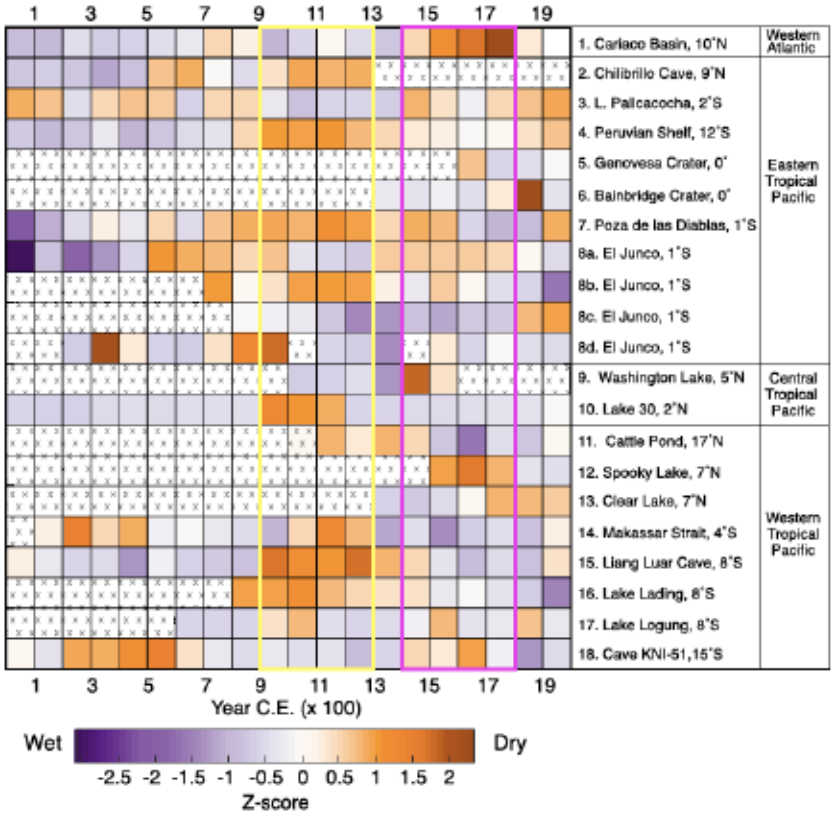

Figure 9. Comparison of tropical Pacific hydroclimate records over the last 2,000 years. All time series were normalized to standard *Z* scores and averaged in century-long intervals. Warm color squares indicate periods inferred to be drier than long-term mean, and cool colors indicate periods inferred to be wetter than long-term mean (based on author interpretations). Vertical boxes indicate approximate time periods for the Medieval Climate Anomaly (900–1300 CE, yellow) and Little Ice Age (1400–1800 CE, magenta). Squares with no data contain an "x" pattern. Site numbers refer to records in Figure 1. Lake 30 data are the S/Ca time series (see Figure 5). Detailed methods for creating this figure are presented in the supporting information (MATLAB; MathWorks Inc., 2016).

coupled ocean-atmosphere dynamics. A cooler Northern Hemisphere during the LIA as a result sof greater volcanic forcing (Atwood et al., 2016) may have shifted the mean ITCZ position southward or caused a contraction from its northern extent in the CTP, whereas a warmer Northern Hemisphere during the MCA, especially in the North Atlantic, a result of enhanced solar forcing (Mann et al., 2009), may have shifted the ITCZ northward. A weaker PWC during the MCA has also been attributed to higher solar irradiance (Yan, Sun, Wang, et al., 2011), whereas a stronger PWC during the MCA could also be due to higher solar irradiance, due to the dynamical thermostat mechanism (Clement et al., 1996). Observations from the CTP do not support any particular forcing possibility; furthermore, it is important to consider that the larger collection of hydroclimate-sensitive proxy records from across the tropical Pacific show no coherent spatiotemporal pattern of hydroclimatic change during these time periods (Figure 10). We note that while spatiotemporal evidence from across the Pacific appears stochastic for the MCA and LIA at this time, unstructured ocean-atmosphere patterns are not the only outcome of unforced climate variability, as structured spatial patterns could arise from internal variability alone (e.g., Wittenberg, 2009). This result indicates the null hypotheses—that centennial-scale changes in hydroclimate across the tropical Pacific are unforced and a result of internal variability (e.g., Ault et al., 2017; PAGES Hydro2k Consortium, 2017)—requires further attention in future studies of the last millennium tropical Pacific hydroclimate.

5. Conclusions

The Kiritimati Lake 30 sediment record, coupled with the record from Washington Lake, ~3° to the north of Kiritimati, provides a southern limit to the possible migration of the CTP ITCZ over the last millennium. Our

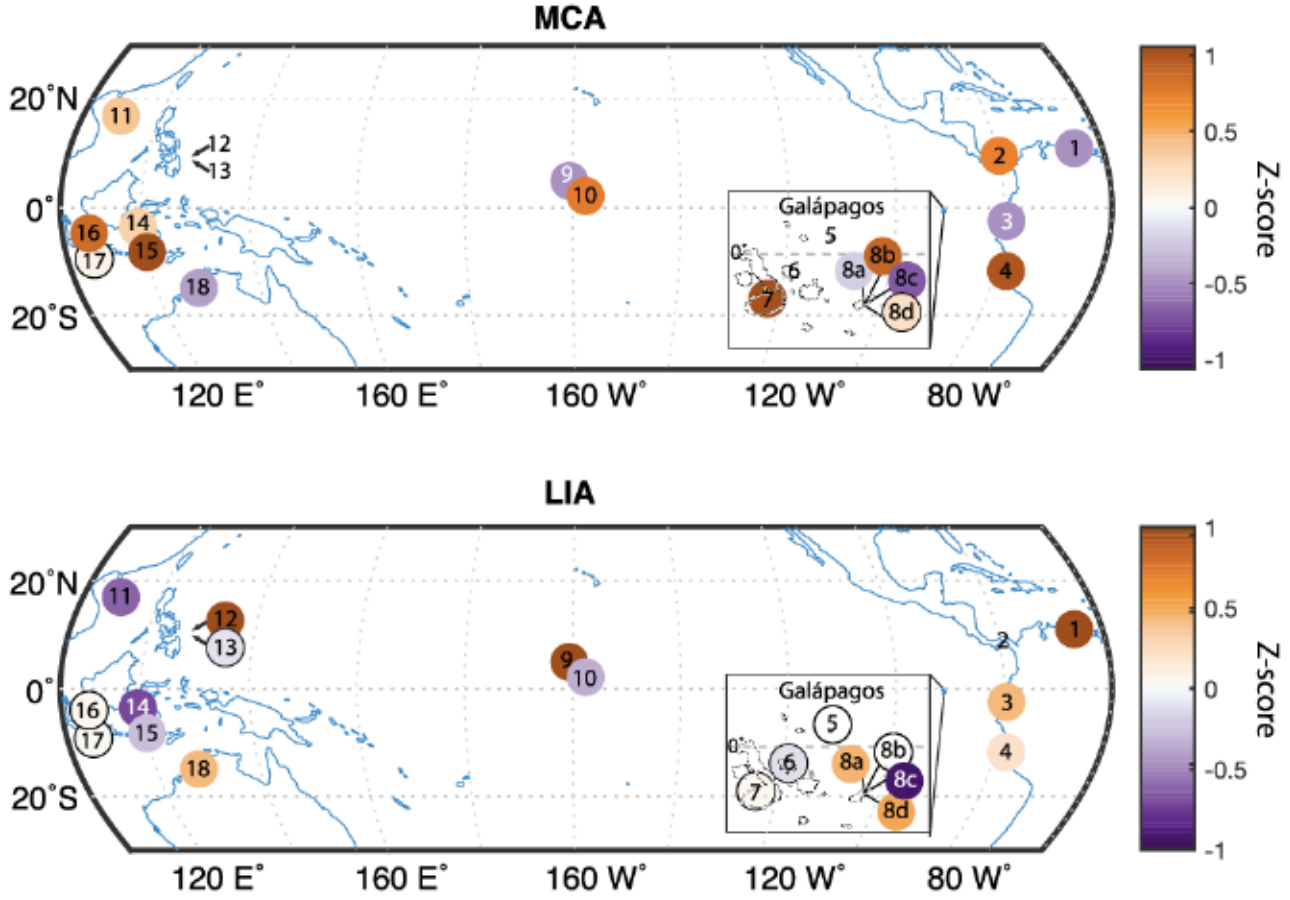

Figure 10. Comparison of tropical Pacific hydroclimate records between the Medieval Climate Anomaly (MCA; 900–1300 CE) and the Little Ice Age (LIA; 1400–1800 CE). All time series were normalized to standard *Z* scores and averaged in century-long intervals, then averaged again for the MCA and LIA intervals. See Figure 9 for the range of hydroclimate *Z* scores within each time period.

record indicates a relatively dry period on Kiritimati Island during the MCA, from 900 to 1200 CE. Evidence of this dry period, coupled with the record from Washington Lake, is consistent with a more northerly position of the CTP ITCZ during the MCA. A gradual shift between 1200 and 1400 CE to sediments similar to modern in Lake 30 and a shift to even drier conditions at Washington Lake at 1420 CE suggest a southward shift of the ITCZ near the beginning of the LIA, relative to its more northerly position during the MCA. Evidence for ITCZ migration in the CTP could support either volcanic or solar forcing mechanisms, via amplifying internal

Table 2
Percent Agreement and Cohen's κ Agreement Statistics for Eight Hydroclimate Hypotheses Tested With Data Set in Figure 9

	All	All	>|0.2|	>|0.2|
Hypothesis	Percent agreement	Cohen's κ	Percent agreement	Cohen's κ
MCA ITCZ northward	1	0.16	0.63	0.14
LIA ITCZ southward	1	0.05	0.64	0.29
MCA PWC stronger	0	0	0.44	0.00
LIA PWC weaker	1	0.01	0.45	0.00
MCA PWC weaker	1	0.19	0.56	0.15
LIA PWC stronger	1	0	0.55	0.10
MCA ITCZ expansion	0	0	0.38	0.00
LIA ITCZ contraction	0.55	0	0.55	0.00

Note. Cohen's κ values <0 are reported as 0. We consider both all available records ("all") and records with strong (>|0.2|) anomalies in the Medieval Climate Anomaly (MCA) and Little Ice Age (LIA; >|0.2|). Although the LIA ends in 1850, due to our century averaging, we average the period 1400–1800 CE. For detailed calculations, see supporting information Data Set 9. ITCZ = Intertropical Convergence Zone, PWC = Pacific Walker Circulation.

coupled ocean-atmosphere dynamics, but a synthesis of 21 hydroclimate-sensitive proxy records from across the tropical Pacific suggests that no singular mechanism is capable of producing the temporal evolution of wet and dry anomalies observed during the MCA and LIA. Nevertheless, as the position and structure of the ITCZ can vary naturally on centennial timescales in the CTP, future changes, either natural, internal, or anthropogenic, will have implications for freshwater resources, drought, and flooding and their impact on the growing population of Kiritimati.

Acknowledgments
This work was funded by NSF-EAR 1602590 and a UIUC Campus Research Board grant to J.L.C. and LacCore support to M.C.H. We are grateful to the Environmental Ministry of the Republic of Kiribati for the research permit to conduct this work. We thank B. Curry, C. Karamperidou, and A. Higley for field assistance and J. Schoonmaker and F. Sansone for helpful discussion. Detailed methods, additional figures and tables supporting our conclusions, and data from this study can be found as supporting information.

References

Adler, R. F., Huffman, G. J., Chang, A., Ferraro, R., Xie, P.-P., Janowiak, J., et al. (2003). The version-2 Global Precipitation Climatology Project (GPCP) monthly precipitation analysis (1979-present). *Journal of Hydrometeorology*, *4*(6), 1147–1167. https://doi.org/10.1175/1525-7541(2003)004%3C1147:TVGPCP%3E2.0.CO;2

Arp, G., Helms, G., Karlinska, K., Schumann, G., Reimer, A., Reitner, J., & Trichet, J. (2012). Photosynthesis versus exopolymer degradation in the formation of microbialites on the atoll of Kiritimati, Republic of Kiribati, Central Pacific. *Geomicrobiology Journal*, *29*(1), 29–65. https://doi.org/10.1080/01490451.2010.521436

Atwood, A. R., & Sachs, J. P. (2014). Separating ITCZ- and ENSO-related rainfall changes in the Galápagos over the last 3 kyr using *D/H* ratios of multiple lipid biomarkers. *Earth and Planetary Science Letters*, *404*, 408–419. https://doi.org/10.1016/j.epsl.2014.07.038

Atwood, A. R., Wu, E., Frierson, D. M. W., Battisti, D. S., & Sachs, J. P. (2016). Quantifying climate forcings and feedbacks over the last millennium in the CMIP5–PMIP3 models. *Journal of Climate*, *29*(3), 1161–1178. https://doi.org/10.1175/JCLI-D-15-0063.1

Ault, T. R., St. George, S., Smerdon, J. E., Coats, S., Mankin, J. S., Carrillo, C. M., et al. (2017). A robust null hypothesis for the potential causes of megadrought in western North America. *Journal of Climate*, *31*(1), 3–24. https://doi.org/10.1175/JCLI-D-17-0154.1

Bethke, C. M., & Yeakel, S. (2016a). *The Geochemist's Workbench® release 11-GWB essentials guide*. Champaign, IL: Aqueous Solutions, LLC.

Bethke, C. M., & Yeakel, S. (2016b). *The Geochemist's Workbench® release 11-GWB reaction modeling guide*. Champaign, IL: Aqueous Solutions, LLC.

Blaauw, M., & Christen, J. A. (2011). Flexible paleoclimate age-depth models using an autoregressive gamma process. *Bayesian Analysis*, *6*(3), 457–474. https://doi.org/10.1214/11-BA618

Clement, A. C., Seager, R., Cane, M. A., & Zebiak, S. E. (1996). An ocean dynamical thermostat. *Journal of Climate*, *9*(9), 2190–2196. https://doi.org/10.1175/1520-0442(1996)009%3C2190:AODT%3E2.0.CO;2

Cohen, J. (1960). A coefficient of agreement for nominal scales. *Educational and Psychological Measurement*, *20*(1), 37–46. https://doi.org/10.1177/001316446002000104

Conroy, J. L., Overpeck, J. T., Cole, J. E., Shanahan, T. M., & Steinitz-Kannan, M. (2008). Holocene changes in eastern tropical Pacific climate inferred from a Galápagos lake sediment record. *Quaternary Science Reviews*, *27*(11–12), 1166–1180. https://doi.org/10.1016/j.quascirev.2008.02.015

Conroy, J. L., Restrepo, A., Overpeck, J. T., Steinitz-Kannan, M., Cole, J. E., Bush, M. B., & Colinvaux, P. A. (2009). Unprecedented recent warming of surface temperatures in the eastern tropical Pacific Ocean. *Nature Geoscience*, *2*(1), 46–50. https://doi.org/10.1038/ngeo390

Conroy, J. L., Thompson, D. M., Collins, A., Overpeck, J. T., Bush, M. B., & Cole, J. E. (2014). Climate influences on water and sediment properties of Genovesa Crater Lake, Galápagos. *Journal of Paleolimnology*, *52*(4), 331–347. https://doi.org/10.1007/s10933-014-9797-z

Cook, H. E., Johnson, P. D., Matti, J. C., & Zemmels, I. (1975). IV. Methods of sample preparation, and X-ray diffraction data analysis, X-Ray Mineralogy Laboratory, Deep Sea Drilling Project, University of California, Riverside. *Initial Reports of the Deep Sea Drilling Project*, *25*. Retrieved from http://deepseadrilling.org/28/volume/dsdp28_appendixIV.pdf

Dean, W. E. (1974). Determination of carbonate and organic matter in calcareous sediments and sedimentary rocks by loss on ignition; Comparison with other methods. *Journal of Sedimentary Research*, *44*(1), 242. https://doi.org/10.1306/74D729D2-2B21-11D7-8648000102C1865D

Denniston, R. F., Ummenhofer, C. C., Wanamaker, A. D., Lachniet, M. S., Villarini, G., Asmerom, Y., et al. (2016). Expansion and contraction of the Indo-Pacific tropical rain belt over the last three millennia. *Scientific Reports*, *6*(1), 34485. https://doi.org/10.1038/srep34485

Dima, I. M., & Wallace, J. M. (2003). On the seasonality of the Hadley cell. *Journal of theAtmospheric Sciences*, *60*(12), 1522–1527. https://doi.org/10.1175/1520-0469(2003)060%3C1522:OTSOTH%3E2.0.CO;2

Dix, G. R., Patterson, R. T., & Park, L. E. (1999). Marine saline ponds as sedimentary archives of late Holocene climate and sea-level variation along a carbonate platform margin: Lee Stocking Island, Bahamas. *Palaeogeography, Palaeoclimatology, Palaeoecology*, *150*(3-4), 223–246. https://doi.org/10.1016/S0031-0182(98)00184-9

Eugster, H. P., & Hardie, L. A. (1978). Saline lakes. In A. Lerman (Ed.), *Lakes: Chemistry, geology, physics* (pp. 237–293). New York: Springer-Verlag. https://doi.org/10.1007/978-1-4757-1152-3_8

Falkland, A. C., & Woodroffe, C. D. (1997). Geology and hydrogeology of Tarawa and Christmas Island, Kiribati. In H. L. Vacher & T. Quinn (Eds.), *Developments in sedimentology* (Vol. 54, pp. 557–610). Amsterdam: Elsevier Science B.V.

Google Earth (2017). Google Earth (version 7.1.8.3036) (data: SIO, NOAA, U.S. Navy, NGA, GEBCO). Digital Globe. Retrieved from https://www.google.com/earth/download/ge/agree.html

Graham, N. E., Hughes, M. K., Ammann, C. M., Cobb, K. M., Hoerling, M. P., Kennett, D. J., et al. (2007). Tropical Pacific – Mid-latitude teleconnections in medieval times. *Climatic Change*, *83*(1-2), 241–285. https://doi.org/10.1007/s10584-007-9239-2

Griffiths, M. L., Kimbrough, A. K., Gagan, M. K., Drysdale, R. N., Cole, J. E., Johnson, K. R., et al. (2016). Western Pacific hydroclimate linked to global climate variability over the past two millennia. *Nature Communications*, *7*, 11719. https://doi.org/10.1038/ncomms11719

Haug, G. H., Hughen, K. A., Sigman, D. M., Peterson, L. C., & Ro, U. (2001). Southward migration of the Intertropical Convergence Zone through the Holocene. *Science*, *293*(5533), 1304–1308. https://doi.org/10.1126/science.1059725

Holding, S., Allen, D. M., Foster, S., Hsieh, A., Larocque, I., Klassen, J., & Van Pelt, S. C. (2016). Groundwater vulnerability on small islands. *Nature Climate Change*, *6*(12), 1100–1103. https://doi.org/10.1038/nclimate3128

Hua, Q., Barbetti, M., & Rakowski, A. Z. (2013). Atmospheric radiocarbon for the period 1950–2010. *Radiocarbon*, *55*(04), 2059–2072. https://doi.org/10.2458/azu_js_rc.v55i2.16177

Kinsman, D. J., & Holland, H. D. (1969). The co-precipitation of cations with CaCO3—IV. The co-precipitation of Sr^{2+} with aragonite between 16° and 96°C. *Geochimica et Cosmochimica Acta*, *33*(1), 1–17. https://doi.org/10.1016/0016-7037(69)90089-1

Konecky, B. L., Russell, J. M., Rodysill, J. R., Vuille, M., Bijaksana, S., & Huang, Y. (2013). Intensification of southwestern Indonesian rainfall over the past millennium. *Geophysical Research Letters, 40*, 386–391. https://doi.org/10.1029/2012GL054331

Lachniet, M. S. (2004). A 1500-year El Niño/Southern Oscillation and rainfall history for the Isthmus of Panama from speleothem calcite. *Journal of Geophysical Research, 109*, D20117. https://doi.org/10.1029/2004JD004694

Last, W. M., & Smol, J. P. (2001). *Tracking environmental change using lake sediments* (Vol. 2). Dordrecht: Kluwer Academic.

Mann, M. E., Zhang, Z., Rutherford, S., Bradley, R. S., Hughes, M. K., Shindell, D., et al. (2009). Global signatures and dynamical origins of the Little Ice Age and Medieval Climate Anomaly. *Science, 326*(5957), 1256–1260. https://doi.org/10.1126/science.1177303

MathWorks Inc. (2016). MATLAB release 2016b MathWorks Inc., Natick, MA.

McDougall, T. J., & Barker, P. M. (2011). Getting started with TEOS-10 and the Gibbs Seawater (GSW) oceanographic toolbox. SCOR/IAPSO WG127.

Moy, C. M., Seltzer, G. O., Rodbell, D. T., & Anderson, D. M. (2002). Variability of El Niño/Southern Oscillation activity at millennial timescales during the Holocene epoch. *Nature, 420*(6912), 162–165. https://doi.org/10.1038/nature01194

Nelson, D. B., & Sachs, J. P. (2016). Galápagos hydroclimate of the Common Era from paired microalgal and mangrove biomarker $^{2}H/^{1}H$ values. *Proceedings of the National Academy of Sciences, 113*(13), 3476–3481. https://doi.org/10.1073/pnas.1516271113

Newton, A., Thunell, R., & Stott, L. (2006). Climate and hydrographic variability in the Indo-Pacific warm pool during the last millennium. *Geophysical Research Letters, 33*, L19710. https://doi.org/10.1029/2006GL027234

PAGES Hydro2k Consortium (2017). Comparing proxy and model estimates of hydroclimate variability and change over the Common Era. *Climate of the Past, 13*(12), 1851–1900. https://doi.org/10.5194/cp-13-1851-2017

Reimer, P. J., Bard, E., Bayliss, A., Beck, J. W., Blackwell, P. G., Ramsey, C. B., et al. (2013). IntCal13 and Marine13 radiocarbon age calibration curves 0–50,000 years cal BP. *Radiocarbon, 55*(04), 1869–1887. https://doi.org/10.2458/azu_js_rc.55.16947

Rein, B., Lückge, A., & Sirocko, F. (2004). A major Holocene ENSO anomaly during the Medieval Period. *Geophysical Research Letters, 31*, L17211. https://doi.org/10.1029/2004GL020161

Richey, J. N., & Sachs, J. P. (2016). Precipitation changes in the western tropical Pacific over the past millennium. *Geology, 44*(8), 671–674. https://doi.org/10.1130/G37822.1

Rodysill, J. R., Russell, J. M., Bijaksana, S., Brown, E. T., Safiuddin, L. O., & Eggermont, H. (2012). A paleolimnological record of rainfall and drought from East Java, Indonesia during the last 1,400 years. *Journal of Paleolimnology, 47*(1), 125–139. https://doi.org/10.1007/s10933-011-9564-3

Sachs, J. P., Sachse, D., Smittenberg, R. H., Zhang, Z., & Battisti, D. S. (2009). Southward movement of the Pacific Intertropical Convergence Zone AD 1400–1850. *Nature Geoscience, 2*. https://doi.org/10.1038/NGEO554

Saenger, C., Miller, M., Smittenberg, R. H., & Sachs, J. P. (2006). A physico-chemical survey of inland lakes and saline ponds: Christmas Island (Kiritimati) and Washington (Teraina) Islands, Republic of Kiribati. *Saline Systems, 2*(1), 1.

Schneider, T., Bischoff, T., & Haug, G. H. (2014). Migrations and dynamics of the Intertropical Convergence Zone. *Nature, 513*(7516), 45–53. https://doi.org/10.1038/nature13636

Schnurrenberger, D., Russell, J., & Kelts, K. (2003). Classification of lacustrine sediments based on sedimentary components. *Journal of Paleolimnology, 29*(2), 141–154. https://doi.org/10.1023/A:1023270324800

Thompson, D. M., Conroy, J. L., Collins, A., Hlohowskyj, S., Overpeck, J. T., Riedinger-Whitmore, M., et al. (2017). Tropical Pacific climate variability over the last 6000 years revealed from Bainbridge Crater Lake, Galápagos. *Paleoceanography, 32*(8), 903–922. https://doi.org/10.1002/2017PA003089

Tierney, J. E., Oppo, D. W., Rosenthal, Y., Russell, J. M., & Linsley, B. K. (2010). Coordinated hydrological regimes in the Indo-Pacific region during the past two millennia. *Paleoceanography, 25*, PA1102. https://doi.org/10.1029/2009PA001871

Trenberth, K. E. (2002). Evolution of El Niño–Southern Oscillation and global atmospheric surface temperatures. *Journal of Geophysical Research, 107*(D8), 4065. https://doi.org/10.1029/2000JD000298

United Nations (2017). World population prospects: The 2017 revision, UN Department of Economic and Social Affairs, Population Division, DVD Edition. Retrieved from http://esa.un.org/unpd/ppp/

Wittenberg, A. T. (2009). Are historical records sufficient to constrain ENSO simulations? *Geophysical Research Letters, 36*, L12702. https://doi.org/10.1029/2009GL038710

Woodroffe, C. D., McGregor, H. V., Lambeck, K., Smithers, S. G., & Fink, D. (2012). Mid-Pacific microatolls record sea-level stability over the past 5000 yr. *Geology, 40*(10), 951–954. https://doi.org/10.1130/G33344.1

Wright, H. E. Jr. (1967). A square-rod piston sampler for lake sediments. *Journal of Sedimentary Research, 37*(3), 975–976. https://doi.org/10.1306/74D71807-2B21-11D7-8648000102C1865D

Yan, H., Sun, L., Oppo, D. W., Wang, Y., Liu, Z., Xie, Z., et al. (2011). South China Sea hydrological changes and Pacific Walker Circulation variations over the last millennium. *Nature Communications, 2*, 293. https://doi.org/10.1038/ncomms1297

Yan, H., Sun, L., Wang, Y., Huang, W., Qiu, S., & Yang, C. (2011). A record of the Southern Oscillation Index for the past 2,000 years from precipitation proxies. *Nature Geoscience, 4*(9), 611–614. https://doi.org/10.1038/ngeo1231

Yan, H., Wei, W., Soon, W., An, Z., Zhou, W., Liu, Z., et al. (2015). Dynamics of the Intertropical Convergence Zone over the western Pacific during the Little Ice Age. *Nature Geoscience, 8*(4), 315–320. https://doi.org/10.1038/ngeo2375

Zaunbrecher, L. K., Cobb, K. M., Beck, J. W., Charles, C. D., Druffel, E. R. M., Fairbanks, R. G., et al. (2010). Coral records of central tropical Pacific radiocarbon variability during the last millennium. *Paleoceanography, 25*, PA4212. https://doi.org/10.1029/2009PA001788